Biomechanics and Modeling in Mechanobiology manuscript No.
(will be inserted by the editor)

Growing skin: Tissue expansion in pediatric forehead reconstruction

Alexander M. Zöllner[1], Adrian Buganza Tepole[1], Arun K. Gosain[2], Ellen Kuhl[1,3,4]

[1] Department of Mechanical Engineering, Stanford University, Stanford, CA 94305, USA
[2] Rainbow Babies and Children's Hospital, Case Western Reserve University, Cleveland, OH 44106, USA
[3] Department of Bioengineering, Stanford University, Stanford, CA 94305, USA
[4] Department of Cardiothoracic Surgery, Stanford University, Stanford, CA 94305, USA

Received: 26.07.11 / Revised version: 13.09.11

Abstract Tissue expansion is a common surgical procedure to grow extra skin through controlled mechanical over-stretch. It creates skin that matches the color, texture, and thickness of the surrounding tissue, while minimizing scars and risk of rejection. Despite intense research in tissue expansion and skin growth, there is a clear knowledge gap between heuristic observation and mechanistic understanding of the key phenomena that drive the growth process. Here, we show that a continuum mechanics approach, embedded in a custom-designed finite element model, informed by medical imaging, provides valuable insight into the biomechanics of skin growth. In particular, we model skin growth using the concept of an incompatible growth configuration. We characterize its evolution in time using a second-order growth tensor parameterized in terms of a scalar-valued internal variable, the in-plane area growth. When stretched beyond the physiological level, new skin is created, and the in-plane area growth increases. For the first time, we simulate tissue expansion on a patient-specific geometric model, and predict stress, strain, and area gain at three expanded locations in a pediatric skull: in the scalp, in the forehead, and in the cheek. Our results may help the surgeon to prevent tissue over-stretch and make informed decisions about expander geometry, size, placement, and inflation. We anticipate our study to open new avenues in reconstructive surgery, and enhance treatment for patients with birth defects, burn injuries, or breast tumor removal.

Key words growth, residual stress, finite element analysis, skin, tissue expansion, reconstructive surgery

1 Motivation

One percent of neonates is born with congenital melanocytic nevi, dark-colored surface lesions present at birth [10]. Congenital nevi may vary in size, shape, texture, color, hairiness, and location, but they have one thing in common: their high malignant potential [23]. Birthmarks larger than 10 cm in diameter are classified as giant congenital nevi and have a prevalence of one in 20,000 infants [45]. Because giant congenital nevi place the child at an increased risk to develop skin cancer, surgical excision remains the standard treatment option [20]. Cosmetic deformity, significant aesthetic disfigurement, and severe psychological distress are additional compelling reasons for nevus removal, especially in the craniofacial region [23].

To reconstruct the defect, preserve function, and maintain aesthetic appearance, tissue expansion has become a major treatment modality in the management of giant congenital nevi [36]. Tissue expansion was first proposed more than half a century ago to reconstruct a traumatic ear and has since then revolutionized reconstructive surgery [43]. Today it is widely used to repair birth defects [5], correct burn injuries [3], and reconstruct breasts after tumor removal [46]. Tissue expansion is the ideal strategy to grow skin that matches the color, texture, hair bearance, and thickness of the surrounding healthy skin, while minimizing scars and risk of rejection [49].

Figure 1, left, shows a one-year old boy who presented with a giant congenital nevus concerning 25 percent of his forehead, extending to the right temporal scalp and cheek [21]. To resurface the nevus region and stimulate in situ skin growth, three simultaneous forehead, cheek, and scalp expanders are used. They are implanted in subcutaneous pockets adjacent to the defect, where they are gradually filled with saline solution. The amount of filling is controlled by visual inspection of skin color and capillary refill [49]. Multiple serial inflations stretch the skin and stimulate tissue growth over a period of several weeks [63]. Once enough skin is created, the expanders are removed, the nevus is excised, and the newly grown skin flaps are advanced to close the defect zone. Figure 1, right, shows the boy at age three, after completed fore-

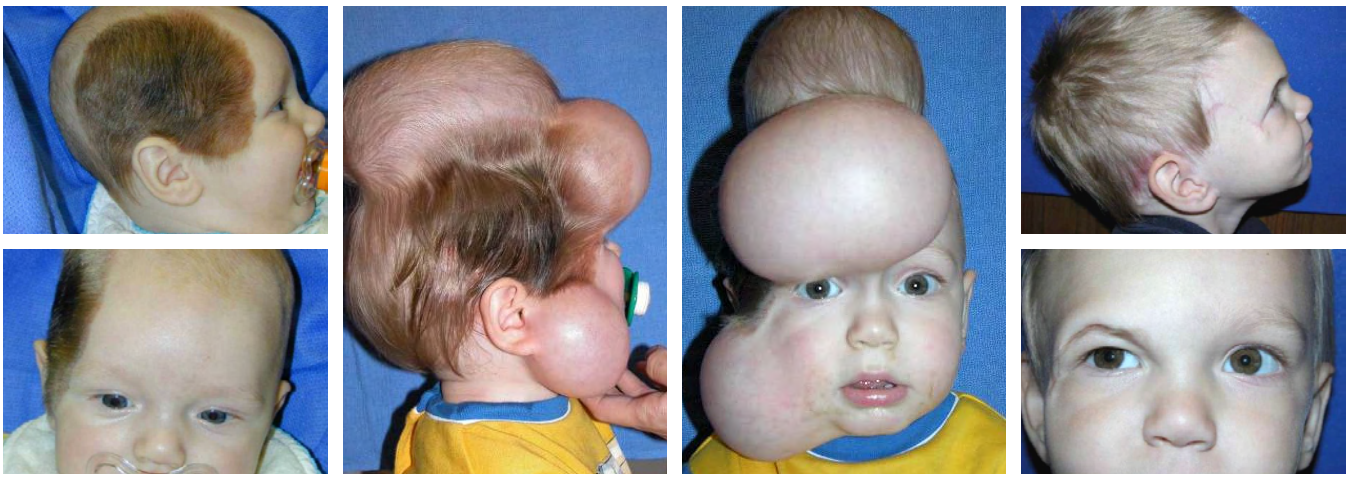

Fig. 1 Tissue expansion for pediatric forehead reconstruction. The patient, a one-year old boy presented with a giant congenital nevus involving 25 percent of his forehead, extending to the right temporal scalp and cheek. Simultaneous forehead, cheek, and scalp expanders were implanted for in situ skin growth. This technique allows to resurface large anatomical areas with skin of similar color, quality, and texture. The follow-up photograph shows the boy at age three, after completed forehead, scalp, and cheek reconstruction.

head, scalp, and cheek reconstruction.

Figure 2 shows a schematic sequence of the mechanical processes during tissue expansion. Initially, at biological equilibrium, the skin is in a natural state of resting tension [54]. When the expander is implanted and inflated, skin is loaded in tension. Stretch beyond a critical level triggers a series of signaling pathways eventually leading to the creation of new skin [57]. On the cellular level, mechanotransduction affects a network of several integrated cascades including growth factors, cytoskeletal rearrangement, and protein kinases [11]. On the tissue level, skin growth induces stress relaxation and restores the state of resting tension [54]. The cycle of expander inflation, stretch, growth, and relaxation is repeated multiple times, typically on a weekly basis [63]. As demonstrated by immunocytochemistry, the expanded tissue undergoes normal cell differentiation and maintains its characteristic phenotype [61]. Skin initially displays thickness changes upon expansion, however, these changes are fully reversible upon expander removal [59]. When the expander is removed, the skin retracts and reveals the irreversible nature of skin growth, associated with growth-induced residual stresses [18,41]. Figure 3 shows a commonly used tissue expander to grow skin in reconstructive surgery.

To predict stress, strain, and area gain during tissue expansion in pediatric forehead reconstruction, we adopt a novel mechanistic approach [8, 9], based on the continuum framework of finite growth [50]. Originally developed for isotropic volumetric growth [14, 37], finite growth theories are based on the multiplicative decomposition of the deformation gradient into an elastic and a growth part [15, 38], a concept adopted from finite

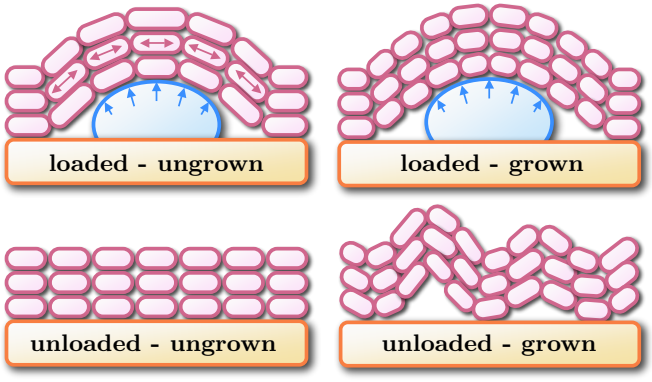

Fig. 2 Schematic sequence of tissue expander inflation. At biological equilibrium, the skin is in a physiological state of resting tension, unloaded and ungrown. When an expander is implanted and inflated, the skin is stretched, loaded and ungrown. Mechanical stretch beyond a critical level triggers a series of signaling pathways eventually leading to the creation of new skin to restore the state of resting tension, loaded and grown. Upon expander removal, elastic deformations retract and inelastic deformations remain, unloaded and grown.

Fig. 3 Tissue expander to grow skin for defect correction in reconstructive surgery. Typical applications are birth defects, burn injuries, and breast reconstruction. Devices consist of a silicone elastomer inflatable expander with a reinforced base for directional expansion, and a remote silicone elastomer injection dome. Courtesy of Mentor Worldwide LLC.

plasticity [34]. Depending on the format of their growth tensor, continuum growth theories have been refined to characterize isotropic [19, 32], transversely isotropic [48,56], orthotropic [17], or generally anisotropic growth [40, 42], either compressible [40] or incompressible [51]. Recent trends focus on the computational modeling of finite growth [22], typically by introducing the growth tensor as an internal variable within a finite element framework [16, 25], a strategy that we also adopt here. A recent monograph that compares different approaches to growth and summarizes the essential findings, trends, and open questions in this progressively evolving new field [2]. Despite ongoing research in growing biological systems, the growth of thin biological membranes remains severely understudied. Only few attempts address the growth of thin biological plates [12] and membranes [40]. Motivated by a first study on axisymmetric skin growth [55], we have recently established a prototype model for growing membranes to predict skin expansion in a general three-dimensional setting [8]. This study capitalizes on recent developments in reconstructive surgery, continuum mechanics of growing tissues, and computational modeling, supplemented by medical image analysis. It documents our first attempts to model and simulate skin expansion in pediatric forehead reconstruction using a real patient-specific geometry.

2 Methods

2.1 Continuum modeling of skin growth

We adopt the kinematics of finite deformations and introduce the deformation map $\boldsymbol{\varphi}$, which, at any given time t maps the material placement $\boldsymbol{X}$ of a physical particle in the material configuration to its spatial placement $\boldsymbol{x}$ in the spatial configuration, $\boldsymbol{x} = \boldsymbol{\varphi}(\boldsymbol{X}, t)$. We choose a formulation which is entirely related to the material frame of reference, and use $\nabla\{\circ\} = \partial_{\boldsymbol{X}}\{\circ\}|_t$ and $\mathrm{Div}\,\{\circ\} = \partial_{\boldsymbol{X}}\{\circ\}|_t : \boldsymbol{I}$ to denote the gradient and the divergence of any field $\{\circ\}(\boldsymbol{X}, t)$ with respect to the material placement $\boldsymbol{X}$ at fixed time t. Here, $\boldsymbol{I}$ is the material identity tensor. To characterize finite growth, we introduce an incompatible growth configuration, and adopt the multiplicative decomposition of the deformation gradient

$$\boldsymbol{F} = \nabla_{\boldsymbol{X}}\boldsymbol{\varphi} = \boldsymbol{F}^{\mathrm{e}} \cdot \boldsymbol{F}^{\mathrm{g}} \tag{1}$$

into a reversible elastic part $\boldsymbol{F}^{\mathrm{e}}$ and an irreversible growth part $\boldsymbol{F}^{\mathrm{g}}$. This multiplicative decomposition, reminiscent of the decomposition of the elastoplastic deformation gradient [34], was first used to describe growth of biologial tissues in [50]. Similarly, we can then decompose the total Jacobian

$$J = \det(\boldsymbol{F}) = J^{\mathrm{e}}\, J^{\mathrm{g}} \tag{2}$$

into an elastic part $J^{\mathrm{e}} = \det(\boldsymbol{F}^{\mathrm{e}})$ and a growth part $J^{\mathrm{g}} = \det(\boldsymbol{F}^{\mathrm{g}})$. We idealize skin as a thin layer characterized through the unit normal $\boldsymbol{n}_0$ in the undeformed reference configuration. The length of the deformed skin normal $\boldsymbol{n} = \mathrm{cof}(\boldsymbol{F}) \cdot \boldsymbol{n}_0 = J\,\boldsymbol{F}^{-\mathrm{t}} \cdot \boldsymbol{n}_0$ introduces the area stretch

$$\vartheta = ||\,\mathrm{cof}(\boldsymbol{F}) \cdot \boldsymbol{n}_0\,|| = \vartheta^{\mathrm{e}}\,\vartheta^{\mathrm{g}} \tag{3}$$

which we can again decompose into an elastic area stretch $\vartheta^{\mathrm{e}} = ||\,\mathrm{cof}(\boldsymbol{F}^{\mathrm{e}}) \cdot \boldsymbol{n}_{\mathrm{g}}/||\boldsymbol{n}_{\mathrm{g}}||\,||$ and a growth area stretch $\vartheta^{\mathrm{g}} = ||\,\mathrm{cof}(\boldsymbol{F}^{\mathrm{g}}) \cdot \boldsymbol{n}_0\,||$ [8]. Here, $\boldsymbol{n}_{\mathrm{g}} = \mathrm{cof}(\boldsymbol{F}^{\mathrm{g}}) \cdot \boldsymbol{n}_0 = J^{\mathrm{g}}\,\boldsymbol{F}^{\mathrm{g}\,-\,\mathrm{t}} \cdot \boldsymbol{n}_0$ denotes the grown skin normal, and $\mathrm{cof}(\circ) = \det(\circ)\,(\circ)^{-\mathrm{t}}$ denotes the cofactor of the second order tensor $(\circ)$. As characteristic deformation measures, we introduce the right Cauchy Green tensor $\boldsymbol{C}$ in the undeformed reference configuration

$$\boldsymbol{C} = \boldsymbol{F}^{\mathrm{t}} \cdot \boldsymbol{F} = \boldsymbol{F}^{\mathrm{gt}} \cdot \boldsymbol{F}^{\mathrm{et}} \cdot \boldsymbol{F}^{\mathrm{e}} \cdot \boldsymbol{F}^{\mathrm{g}} \tag{4}$$

and its elastic counterpart $\boldsymbol{C}^{\mathrm{e}} = \boldsymbol{F}^{\mathrm{et}} \cdot \boldsymbol{F}^{\mathrm{e}} = \boldsymbol{F}^{\mathrm{g}\,-\,\mathrm{t}} \cdot \boldsymbol{C} \cdot \boldsymbol{F}^{\mathrm{g}\,-\,1}$ in the intermediate configuration. This allows us to rephrase the total area stretch as $\vartheta = J\,[\,\boldsymbol{n}_0 \cdot \boldsymbol{C}^{-1} \cdot \boldsymbol{n}_0\,]^{1/2}$. Finally, we introduce the pull back of the spatial velocity gradient $\boldsymbol{l} = \dot{\boldsymbol{F}} \cdot \boldsymbol{F}^{-1}$ to the intermediate configuration,

$$\boldsymbol{F}^{\mathrm{e}\,-\,1} \cdot \boldsymbol{l} \cdot \boldsymbol{F}^{\mathrm{e}} = \boldsymbol{L}^{\mathrm{e}} + \boldsymbol{L}^{\mathrm{g}} \tag{5}$$

which obeys the additive decomposition into the elastic velocity gradient $\boldsymbol{L}^{\mathrm{e}} = \boldsymbol{F}^{\mathrm{e}-1} \cdot \dot{\boldsymbol{F}}^{\mathrm{e}}$ and the growth velocity gradient $\boldsymbol{L}^{\mathrm{g}} = \dot{\boldsymbol{F}}^{\mathrm{g}} \cdot \boldsymbol{F}^{\mathrm{g}-1}$. Here, $\{\dot{\circ}\} = \partial_t\{\circ\}|_{\boldsymbol{X}}$ denotes the material time derivative of any field $\{\circ\}(\boldsymbol{X}, t)$ at fixed material placement $\boldsymbol{X}$.

We characterize growing tissue using the framework of open system thermodynamics in which the material density ρ_0 is allowed to change as a consequence of growth [26, 28]. The balance of mass for open systems balances its rate of change $\dot{\rho}_0$ with a possible in- or outflux of mass $\boldsymbol{R}$ and mass source $\mathcal{R}_0$ [29, 44].

$$\dot{\rho}_0 = \mathrm{Div}\,(\boldsymbol{R}) + \mathcal{R}_0 \tag{6}$$

Similarly, the balance of linear momentum balances the density-weighted rate of change of the velocity $\rho_0\,\boldsymbol{v} = \rho_0\,\dot{\boldsymbol{\varphi}}$, with the momentum flux $\boldsymbol{P} = \boldsymbol{F} \cdot \boldsymbol{S}$, and the momentum source $\rho_0\,\boldsymbol{b}$,

$$\rho_0\,\dot{\boldsymbol{v}} = \mathrm{Div}\,(\boldsymbol{F} \cdot \boldsymbol{S}) + \rho_0\,\boldsymbol{b} \tag{7}$$

here stated in its mass-specific form [27]. $\boldsymbol{P}$ and $\boldsymbol{S}$ are the first and second Piola-Kirchhoff stress tensors. Last, we would like to point out that the dissipation inequality for open systems

$$\rho_0\,\mathcal{D} = \boldsymbol{S} : \tfrac{1}{2}\dot{\boldsymbol{C}} - \rho_0\,\dot{\psi} - \rho_0\,\mathcal{S} \geq 0 \tag{8}$$

typically contains an extra entropy source $\rho_0\,\mathcal{S}$ to account for the growing nature of living biological systems [26, 41]. Equations (7) and (8) represent the mass-specific versions of the balance of momentum and of the

dissipation inequality which are particularly useful in the context of growth since they contains no explicit dependencies on the changes in mass [27].

To close the set of equations, we introduce the constitutive equations for the mass source $\mathcal{R}_0$, for the momentum flux $\boldsymbol{S}$, and for the growth tensor $\boldsymbol{F}^{\mathrm{g}}$, assuming that the mass flux $\boldsymbol{R} = \boldsymbol{0}$, the momentum source $\boldsymbol{b} = \boldsymbol{0}$, and the acceleration $\dot{\boldsymbol{v}} = \boldsymbol{0}$ are negligibly small. On the cellular level, immunocytochemistry has shown that expanded tissue undergoes normal epidermal cell differentiation [61]. On the organ level, mechanical testing has confirmed that the newly grown skin has the same material properties as the initial tissue [63]. Accordingly, we assume that the newly grown skin has the same density as the initial tissue. This implies that the mass source

$$\mathcal{R}_0 = \rho_0 \, \mathrm{tr}\,(\boldsymbol{L}^{\mathrm{g}}) \tag{9}$$

can be expressed as the density-weighted trace of the growth velocity gradient $\mathrm{tr}\,(\boldsymbol{L}^{\mathrm{g}}) = \dot{\boldsymbol{F}}^{\mathrm{g}} : \boldsymbol{F}^{\mathrm{g}\,-\mathrm{t}}$ [22]. We model skin as a hyperelastic material characterized through the Helmholtz free energy $\psi = \hat{\psi}\,(\boldsymbol{C}, \boldsymbol{F}^{\mathrm{g}})$, which we use to evaluate the dissipation inequality (8).

$$\rho_0 \mathcal{D} = \left[\boldsymbol{S} - \rho_0 \frac{\partial \psi}{\partial \boldsymbol{C}} \right] : \tfrac{1}{2} \dot{\boldsymbol{C}} + \boldsymbol{M}^{\mathrm{e}} : \boldsymbol{L}^{\mathrm{g}} - \rho_0 \frac{\partial \psi}{\partial \rho_0} \mathcal{R}_0 - \rho_0 \mathcal{S}_0 \geq 0 \tag{10}$$

We observe that the Mandel stress of the intermediate configuration $\boldsymbol{M}^{\mathrm{e}} = \boldsymbol{C}^{\mathrm{e}} \cdot \boldsymbol{S}^{\mathrm{e}}$ is energetically conjugate to the growth velocity gradient $\boldsymbol{L}^{\mathrm{g}} = \dot{\boldsymbol{F}}^{\mathrm{g}} \cdot \boldsymbol{F}^{\mathrm{g}\,-1}$. From the dissipation inequality (10), we obtain the definition of the second Piola Kirchhoff stress $\boldsymbol{S}$ as thermodynamically conjugate quantity to the right Cauchy Green deformation tensor $\boldsymbol{C}$.

$$\boldsymbol{S} = 2\,\rho_0 \, \frac{\partial \psi}{\partial \boldsymbol{C}} = 2 \frac{\partial \psi}{\partial \boldsymbol{C}^{\mathrm{e}}} : \frac{\partial \boldsymbol{C}^{\mathrm{e}}}{\partial \boldsymbol{C}} = \boldsymbol{F}^{\mathrm{g}\,-1} \cdot \boldsymbol{S}^{\mathrm{e}} \cdot \boldsymbol{F}^{\mathrm{g}\,-\mathrm{t}} \tag{11}$$

According to this definition, the first derivative of the Helmholtz free energy ψ with respect to the elastic right Cauchy Green tensor $\boldsymbol{C}^{\mathrm{e}}$ introduces the elastic second Piola Kirchhoff stress $\boldsymbol{S}^{\mathrm{e}}$, while the second derivative defines the elastic constitutive moduli $\mathbb{L}^{\mathrm{e}}$.

$$\boldsymbol{S}^{\mathrm{e}} = 2\,\rho_0 \, \frac{\partial \psi}{\partial \boldsymbol{C}^{\mathrm{e}}} \quad \text{and} \quad \mathbb{L}^{\mathrm{e}} = 2 \, \frac{\partial \boldsymbol{S}^{\mathrm{e}}}{\partial \boldsymbol{C}^{\mathrm{e}}} = 4\,\rho_0 \, \frac{\partial^2 \psi}{\partial \boldsymbol{C}^{\mathrm{e}} \otimes \partial \boldsymbol{C}^{\mathrm{e}}} \tag{12}$$

To focus on the impact of growth, rather than adopting a sophisticated anisotropic material model for skin [9,30], we assume a classical Neon-Hookean free energy $\rho_0\,\psi = \frac{1}{2}\,\lambda\,\ln^2(J^{\mathrm{e}}) + \frac{1}{2}\,\mu\,[\,\boldsymbol{C}^{\mathrm{e}} : \boldsymbol{I} - 3 - 2\,\ln(J^{\mathrm{e}})\,]$, introducing the elastic second Piola Kirchhoff stress $\boldsymbol{S}^{\mathrm{e}} = [\,\lambda\,\ln(J^{\mathrm{e}}) - \mu\,]\,\boldsymbol{C}^{\mathrm{e}\,-1} + \mu\,\boldsymbol{I}$, and the elastic constitutive moduli $\mathbb{L}^{\mathrm{e}} = \lambda\,\boldsymbol{C}^{\mathrm{e}\,-1} \otimes \boldsymbol{C}^{\mathrm{e}\,-1} + [\,\mu - \lambda\,\ln(J^{\mathrm{e}})\,]\,[\,\boldsymbol{C}^{\mathrm{e}} \overline{\otimes} \boldsymbol{C}^{\mathrm{e}} + \boldsymbol{C}^{\mathrm{e}} \underline{\otimes} \boldsymbol{C}^{\mathrm{e}}\,]$. Motivated by clinical observations [49], we classify skin growth as a strain-driven, transversely isotropic, irreversible process. It is characterized through one single growth multiplier ϑ^{g} that reflects the irreversible area increase perpendicular to the skin normal $\boldsymbol{n}_0$.

$$\boldsymbol{F}^{\mathrm{g}} = \sqrt{\vartheta^{\mathrm{g}}}\,\boldsymbol{I} + [\,1 - \sqrt{\vartheta^{\mathrm{g}}}\,]\,\boldsymbol{n}_0 \otimes \boldsymbol{n}_0 \tag{13}$$

For this particular type of transversely isotropic growth, for which all thickness changes are reversibly elastic [59], area growth is identical to volume growth, i.e., $\vartheta^{\mathrm{g}} = \det(\boldsymbol{F}^{\mathrm{g}}) = J^{\mathrm{g}}$. Because of the simple rank-one update structure in (13), we can invert the growth tensor explicitly, $\boldsymbol{F}^{\mathrm{g}\,-1} = 1/\sqrt{\vartheta^{\mathrm{g}}}\,\boldsymbol{I} + [\,1 - 1/\sqrt{\vartheta^{\mathrm{g}}}\,]\,\boldsymbol{n}_0 \otimes \boldsymbol{n}_0$, using the Sherman-Morrison formula. This explicit representation introduces the following simple expression for the growth velocity gradient,

$$\boldsymbol{L}^{\mathrm{g}} = \sqrt{\dot{\vartheta}^{\mathrm{g}}}/\sqrt{\vartheta^{\mathrm{g}}}\,\boldsymbol{I} + [\,1 - \sqrt{\dot{\vartheta}^{\mathrm{g}}}/\sqrt{\vartheta^{\mathrm{g}}}\,]\,\boldsymbol{n}_0 \otimes \boldsymbol{n}_0 \tag{14}$$

which proves convenient to explicitly evaluate the mass source in equation (9) as $\mathcal{R}_0 = \rho_0\,[\,1 + 2\,\sqrt{\dot{\vartheta}^{\mathrm{g}}}/\sqrt{\vartheta^{\mathrm{g}}}\,]$. Motivated by physiological observations of stretch-induced skin expansion [21], we adopt the following evolution equation for the growth multiplier,

$$\dot{\vartheta}^{\mathrm{g}} = k^{\mathrm{g}}(\vartheta^{\mathrm{g}})\,\phi^{\mathrm{g}}(\vartheta^{\mathrm{e}}) \tag{15}$$

which follows a well-established functional form [37], but is now rephrased in a strain-driven format [17]. To control unbounded growth, we introduce the weighting function

$$k^{\mathrm{g}} = \frac{1}{\tau} \, \left[\frac{\vartheta^{\max} - \vartheta^{\mathrm{g}}}{\vartheta^{\max} - 1} \right]^{\gamma} \tag{16}$$

where $1/\tau$ controls the adaptation speed, the exponent γ calibrates the shape of the growth curve, and $\vartheta^{\max} > 1$ is the maximum area growth [22,37]. The growth criterion

$$\phi^{\mathrm{g}} = \left\langle \vartheta^{\mathrm{e}} - \vartheta^{\mathrm{crit}} \right\rangle = \left\langle \vartheta/\vartheta^{\mathrm{g}} - \vartheta^{\mathrm{crit}} \right\rangle \tag{17}$$

is driven by the elastic area stretch $\vartheta^{\mathrm{e}} = \vartheta/\vartheta^{\mathrm{g}}$, such that growth is activated only if the elastic area stretch exceeds a critical physiological stretch limit $\vartheta^{\mathrm{crit}}$. Here, $\langle \circ \rangle$ denote the Macaulay brackets.

Figure 4 displays the constitutive response of the four-parameter growth model in equi-biaxial stretch. At a prescribed piecewise constant total stretch ϑ, the growth stretch ϑ^{g} increases gradually while the elastic stretch ϑ^{e}decreases. This induces stress relaxation. Horizontal dashed lines represent the elastic stretch limit beyond which skin growth is activated $\vartheta^{\mathrm{crit}}$ and the maximum area growth $\vartheta^{\max}$. Increased adaptation speeds $1/\tau \uparrow$ and decreased growth exponents $\gamma \downarrow$ both accelerate convergence towards the biological equilibrium [22], but do not affect the final equilibrium state [48, 51]. At all times, the multiplicative decomposition of the deformation gradient $\boldsymbol{F} = \boldsymbol{F}^{\mathrm{e}} \cdot \boldsymbol{F}^{\mathrm{g}}$ introduced in equation (1) carries over to the multiplicative decomposition of the total area stretch $\vartheta = \vartheta^{\mathrm{e}}\,\vartheta^{\mathrm{g}}$ of equation (3).

2.2 Computational modeling of skin growth

We solve the coupled biological and mechanical equilibrium for skin growth within an incremental iterative finite element setting [58]. To characterize the growth

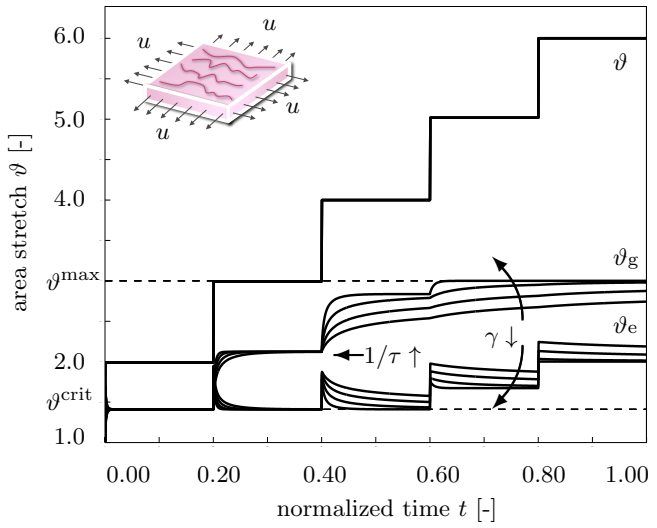

Fig. 4 Tissue expansion in equi-biaxial stretch. Temporal evolution of total, elastic, and growth area stretch ϑ, ϑ^{e}, and ϑ^{g} for displacement driven skin expansion at varying growth exponents γ. At a piecewise constant total stretch, the growth stretch increases gradually while the elastic stretch decreases. This induces stress relaxation. Horizontal dashed lines represent the elastic stretch limit beyond which skin growth is activated ϑ^{crit}, and the maximum area growth $\vartheta^{\max}$.

process at each instant in time, we introduce the growth multiplier ϑ^{g} as an internal variable, and solve the biological equilibrium (15) locally at the integration point level. For the temporal discretization, we partition the time interval of interest $\mathcal{T}$ into n_{stp} subintervals, $\mathcal{T} = \mathop{\mathbf{U}}_{\text{n}=1}^{\text{n}_{\text{stp}}} [\, t_{\text{n}}, t_{\text{n}+1} \,]$ and focus on the interval $[\, t_{\text{n}}, t_{\text{n}+1} \,]$ for which $\Delta t = t_{\text{n}+1} - t_{\text{n}} > 0$ denotes the current time increment. Our goal is to determine the current growth multiplier ϑ^{g} for a given deformation state $\boldsymbol{F}$ at time t, and a given growth multiplier $\vartheta^{\text{g}}_{\text{n}}$ at the end of the previous time step t_{n}. For the sake of compactness, we omit the index $(\circ)_{\text{n}+1}$ for all quantities at the end of the current time step $t_{\text{n}+1}$. We evaluate the material time derivative of the growth multiplier $\dot{\vartheta}^{\text{g}} = [\, \vartheta^{\text{g}} - \vartheta^{\text{g}}_{\text{n}} \,] \,/\, \Delta t$ using a finite difference approximation. In the spirit of implicit time integration schemes, we now reformulate the evolution equation (15), introducing the discrete residual R^{ϑ} in terms of the unknown growth multiplier ϑ^{g}.

$$\mathsf{R}^{\vartheta} = \vartheta^{\text{g}} - \vartheta^{\text{g}}_{\text{n}} - k^{\text{g}}\, \phi^{\text{g}}\, \Delta t \doteq 0 \tag{18}$$

We solve this nonlinear residual equation using a local Newton iteration. Within each iteration step, we calculate the linearization of the residual R^{ϑ} with respect to the growth multiplier ϑ^{g},

$$\mathsf{K}^{\vartheta} = \frac{\partial \mathsf{R}^{\vartheta}}{\partial \vartheta^{\text{g}}} = 1 - \left[\frac{\partial k^{\text{g}}}{\partial \vartheta^{\text{g}}}\, \phi^{\text{g}} + k^{\text{g}}\, \frac{\partial \phi^{\text{g}}}{\partial \vartheta^{\text{g}}} \right] \Delta t \tag{19}$$

with the derivatives of the weighting function $\partial k^{\text{g}} / \partial \vartheta^{\text{g}} = -\,\gamma\, k \,/\, [\, \vartheta^{\max} - \vartheta^{\text{g}} \,]$ and the growth criterion $\partial \phi^{\text{g}} / \partial \vartheta^{\text{g}} = -\,\vartheta \,/\, \vartheta^{\text{g}\,2}$ introduced in equations (16) and (17). Within each iteration step, we iteratively update the unknown growth multiplier $\vartheta^{\text{g}} \leftarrow \vartheta^{\text{g}} - \mathsf{R}^{\vartheta} \,/\, \mathsf{K}^{\vartheta}$ until convergence is achieved, i.e., until the local growth update $\Delta \vartheta^{\text{g}} = -\mathsf{R}^{\vartheta} \,/\, \mathsf{K}^{\vartheta}$ reaches a user-defined tolerance.

To explore the interplay between growth and mechanics, we discretize the deformation map $\boldsymbol{\varphi}$ as nodal degree of freedom, and solve the mechanical equilibrium (7) globally at the node point level. To solve the quasi-static mechanical equilibrium, $\text{Div}\,(\boldsymbol{F} \cdot \boldsymbol{S}) = \boldsymbol{0}$, we cast it into its weak form, $\int_{\mathcal{B}_0} \nabla \delta\boldsymbol{\varphi} : [\, \boldsymbol{F} \cdot \boldsymbol{S} \,]\, \text{d}V = 0$, through multiplication with the test function $\delta\boldsymbol{\varphi}$ and integration over the domain of interest $\mathcal{B}_0$. For the spatial discretization, we partition the domain of interest $\mathcal{B}_0 = \mathop{\mathbf{U}}_{\text{e}=1}^{\text{n}_{\text{el}}} \mathcal{B}^{\text{e}}_0$ into n_{el} finite elements $\mathcal{B}^{\text{e}}_0$. Our goal is to determine the deformation state $\boldsymbol{\varphi}$ for a given load at time t. To approximate the test function $\delta\boldsymbol{\varphi} = \sum_{i=1}^{\text{n}_{\text{en}}} N^i\, \delta\boldsymbol{\varphi}_i$, the unknown deformation $\boldsymbol{\varphi} = \sum_{j=1}^{\text{n}_{\text{en}}} N^j\, \delta\boldsymbol{\phi}_j$, and their gradients $\nabla\delta\boldsymbol{\varphi} = \sum_{i=1}^{\text{n}_{\text{en}}} \delta\boldsymbol{\varphi}_i \otimes \nabla N^i \boldsymbol{\varphi}$ and $\nabla\boldsymbol{\varphi} \sum_{j=1}^{\text{n}_{\text{en}}} \boldsymbol{\varphi}_j \otimes \nabla N^j$, we apply an isoparametric Bubnov-Galerkin based finite element interpolation, where N^i and N^j are the element shape functions and $i, j = 1, .., \text{n}_{\text{en}}$ are the element nodes. We now reformulate the weak form of the balance of linear momentum (7) with the help of these finite element approximations, introducing the discrete residual $\mathbf{R}^{\varphi}_I$ in terms of the unknown nodal deformation $\boldsymbol{\varphi}_J$.

$$\mathbf{R}^{\varphi}_I = \mathop{\mathbf{A}}_{\text{e}=1}^{\text{n}_{\text{el}}} \int_{\mathcal{B}_{\text{e}}} \nabla N^i_{\varphi} \cdot [\, \boldsymbol{F} \cdot \boldsymbol{S} \,]\, \text{d}V_{\text{e}} \doteq \boldsymbol{0} \tag{20}$$

Here, the operator $\mathbf{A}$ symbolizes the assembly of all element residuals at the $j = 1, .., \text{n}_{\text{en}}$ element nodes to the global residual at the global node points $J = 1, .., \text{n}_{\text{el}}$. We evaluate the global discrete residual (20), once we have iteratively determined the growth multiplier ϑ^{g} for the given deformation state $\boldsymbol{F}$ and the given history $\vartheta^{\text{g}}_{\text{n}}$ as described in the previous section. Then we successively determine the growth tensor $\boldsymbol{F}^{\text{g}}$ from equation (13), the elastic tensor $\boldsymbol{F}^{\text{e}} = \boldsymbol{F} \cdot \boldsymbol{F}^{\text{g}\,-1}$ from equation (1), the elastic stress $\boldsymbol{S}^{\text{e}}$ from equation (12), and lastly, the second Piola Kirchhoff stress $\boldsymbol{S}$ from equation (11). Again, we suggest an incremental iterative Newton algorithm to solve the nonlinear residual equation for the unknown deformation (20). The consistent linearization of the residual $\mathbf{R}^{\varphi}_I$ with respect to the nodal vector of unknowns $\boldsymbol{\varphi}_J$ introduces the global stiffness matrix.

$$\begin{aligned} \mathbf{K}^{\varphi}_{IJ} = \frac{\partial \mathbf{R}^{\varphi}_I}{\partial \boldsymbol{\varphi}_J} = \mathop{\mathbf{A}}_{\text{e}=1}^{\text{n}_{\text{el}}} \int_{\mathcal{B}_{\text{e}}} & \nabla N^i_{\varphi} \cdot \boldsymbol{S} \cdot \nabla N^j_{\varphi}\, \boldsymbol{I} \\ & + [\nabla N^i_{\varphi} \cdot \boldsymbol{F}]^{\text{sym}} \cdot \mathbf{L} \cdot [\boldsymbol{F}^{\text{t}} \cdot \nabla N^j_{\varphi}]^{\text{sym}} \text{d}V_{\text{e}} \end{aligned} \tag{21}$$

The fourth order tensor $\mathbf{L}$ denotes the Lagrangian constitutive moduli which, we can determine directly from the linearization of the Piola Kirchhoff stress $\boldsymbol{S}$ with respect to the total right Cauchy Green tensor $\boldsymbol{C}$ [16].

$$\mathbf{L} = 2\, \frac{\text{d}\boldsymbol{S}}{\text{d}\boldsymbol{C}} = 2\, \frac{\partial \boldsymbol{S}}{\partial \boldsymbol{C}}\bigg|_{\boldsymbol{F}^{\text{g}}} + 2 \left[\frac{\partial \boldsymbol{S}}{\partial \boldsymbol{F}^{\text{g}}} : \frac{\partial \boldsymbol{F}^{\text{g}}}{\partial \vartheta^{\text{g}}} \right] \otimes \frac{\partial \vartheta^{\text{g}}}{\partial \boldsymbol{C}}\bigg|_{\boldsymbol{F}} \tag{22}$$

The first term

$$2\,\frac{\partial \boldsymbol{S}}{\partial \boldsymbol{C}} = [\,\boldsymbol{F}^{\mathrm{g}\,-1}\overline{\otimes}\,\boldsymbol{F}^{\mathrm{g}\,-1}\,] : \mathsf{L}^{\mathrm{e}} : [\,\boldsymbol{F}^{\mathrm{g}\,-\mathrm{t}}\overline{\otimes}\,\boldsymbol{F}^{\mathrm{g}\,-\mathrm{t}}\,] \quad (23)$$

represents the pull back of the elastic moduli L^{e} introduced in equation (12) onto the reference configuration. Here we have used the abbreviations $\{\bullet\overline{\otimes}\circ\}_{ijkl} = \{\bullet\}_{ik}\ \{\circ\}_{jl}$ and $\{\bullet\underline{\otimes}\circ\}_{ijkl} = \{\bullet\}_{il}\ \{\circ\}_{jk}$ for the non-standard fourth order products. The second term

$$\begin{aligned}\frac{\partial \boldsymbol{S}}{\partial \boldsymbol{F}^{\mathrm{g}}} =& -[\,\boldsymbol{F}^{\mathrm{g}-1}\,\overline{\otimes}\,\boldsymbol{S} + \boldsymbol{S}\,\underline{\otimes}\,\boldsymbol{F}^{\mathrm{g}-1}\,] \\ & -[\boldsymbol{F}^{\mathrm{g}-1}\overline{\otimes}\boldsymbol{F}^{\mathrm{g}-1}] : \tfrac{1}{2}\mathsf{L}^{\mathrm{e}} : [\boldsymbol{F}^{\mathrm{g}-\mathrm{t}}\underline{\otimes}\boldsymbol{C}^{\mathrm{e}} + \boldsymbol{C}^{\mathrm{e}}\overline{\otimes}\boldsymbol{F}^{\mathrm{g}-\mathrm{t}}]\end{aligned} \quad (24)$$

consists of two terms that resemble a geometric and a material stiffness in nonlinear continuum mechanics. The third term

$$\frac{\partial \boldsymbol{F}^{\mathrm{g}}}{\partial \vartheta^{\mathrm{g}}} = \frac{1}{2\,\sqrt{\vartheta^{\mathrm{g}}}}\,[\,\boldsymbol{I} - \boldsymbol{n}_0 \otimes \boldsymbol{n}_0\,] \quad (25)$$

and the fourth term

$$\begin{aligned}\frac{\partial \vartheta^{\mathrm{g}}}{\partial \boldsymbol{C}} =& \frac{1}{\tau}\frac{1}{\vartheta^{\mathrm{g}}}\left[\frac{\vartheta^{\max} - \vartheta^{\mathrm{g}}}{\vartheta^{\max} - 1}\right]^{\gamma}\frac{1}{\mathsf{K}^{\mathrm{g}}}\,\Delta t \\ & \frac{1}{2}\,\vartheta\,\boldsymbol{C}^{-1} - \frac{1}{2}\,\frac{J^2}{\vartheta}[\boldsymbol{C}^{-1}\cdot\boldsymbol{n}_0] \otimes [\boldsymbol{C}^{-1}\cdot\boldsymbol{n}_0]\end{aligned} \quad (26)$$

depend on the particular choice for the growth tensor $\boldsymbol{F}^{\mathrm{g}}$ in equation (13) and on the evolution equation for the growth multiplier ϑ^{g} in equation (15), respectively. For each global Newton iteration step, we iteratively update the current deformation state $\boldsymbol{\varphi} \leftarrow \boldsymbol{\varphi} - \mathsf{K}^{\varphi\,-1}_{IJ}\cdot\mathsf{R}^{\varphi}_{I}$ until we achieve algorithmic convergence. Upon convergence, we store the corresponding growth multipliers ϑ^{g} at the integration point level. Table 1 summarizes the algorithmic treatment of skin growth at the integration point level.

Table 1 Algorithmic flowchart for strain-driven transversely isotropic area growth.

given $\boldsymbol{F}$ and $\vartheta^{\mathrm{g}}_{\mathrm{n}}$	
initialize $\vartheta^{\mathrm{g}} \leftarrow \vartheta^{\mathrm{g}}_{\mathrm{n}}$	
local Newton iteration	
check growth criterion $\phi^{\mathrm{g}} = \vartheta^{\mathrm{e}} - \vartheta^{\mathrm{crit}} \geq 0$?	(17)
calculate residual $\mathsf{R} = \vartheta^{\mathrm{g}} - \vartheta^{\mathrm{g}}_{\mathrm{n}} - k^{\mathrm{g}}\,\phi^{\mathrm{g}}\Delta t$	(18)
calculate tangent $\mathsf{K} = \partial\mathsf{R}\,/\,\partial\vartheta^{\mathrm{g}}$	(19)
update growth stretch $\vartheta^{\mathrm{g}} \leftarrow \vartheta^{\mathrm{g}} - \mathsf{R}\,/\,\mathsf{K}$	
check convergence $\mathsf{R} \leq$ tol ?	
calculate growth tensor $\boldsymbol{F}^{\mathrm{g}}$	(13)
calculate elastic tensor $\boldsymbol{F}^{\mathrm{e}} = \boldsymbol{F}\cdot\boldsymbol{F}^{\mathrm{g}\,-1}$	(1)
calculate elastic right Cauchy Green tensor $\boldsymbol{C}^{\mathrm{e}}$	(4)
calculate elastic second Piola Kirchhoff stress $\boldsymbol{S}^{\mathrm{e}}$	(12)
calculate second Piola Kirchhoff stress $\boldsymbol{S}$	(11)
calculate Lagrangian moduli L	(22)

2.3 Geometric modeling of skin growth

To simulate skin growth on an anatomically exact geometry, we create a finite element mesh on the basis of three-dimensional computer tomography images shown in Figure 5. Figure 6 summarizes the sequence of steps to generate our patient-specific geometric model. First, we identify the skin region by a distinct grey scale value in the computer tomography scans and extract point cloud data of its boundary. Figure 6, left, mimics the discrete nature of the extracted point cloud, with high point densities in the scanning plane and low point densities between the distinct planes. To smoothen the data and decreases the overall number of points, we homogenize the point cloud using a median filter. Next, we create a triangular surface mesh from the smoothened point cloud by applying a ball-pivoting algorithm [7]. Ball-pivoting algorithms are particularly suited for surface reconstruction of large data sets. After placing an initial seed element, the ball-pivoting algorithm rotates a sphere over the edges of this element and sequentially creates new elements whenever the sphere touches three data points. However, since our data are based on plane-wise computer tomography scans, ball-pivoting algorithms typically fail to automatically create smooth surfaces. Unfortunately, other fully automated meshing strategies such as convex hull or shrink wrap algorithms are not suitable for non-convex geometries like the face, which possesses several non-convexities in the eye, nose, mouth, and ear regions [24]. Accordingly, we smoothen the triangular surface mesh semi-manually, as illustrated in Figure 6, middle.

From the smoothened surface mesh, we finally create a one-element thick volume mesh of the pediatric skull, discretized with 61,228 nodes, 183,684 degrees of freedom, and 30,889 tri-linear brick elements. As a first approximation, we assume that all eight integration points within each element posses the same skin plane normal $\boldsymbol{n}_0$, corresponding to the normal from the initial surface mesh. We virtually implant three tissue expanders as shown in Figure 6, right, motivated by the tissue ex-

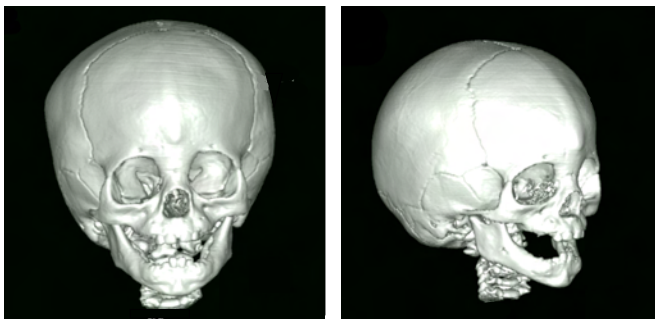

Fig. 5 Three-dimensional computer tomography scans from the skull of a one-year old child. We create a patient-specific geometric model using discrete boundary points extracted from sliced image sections across the skull.

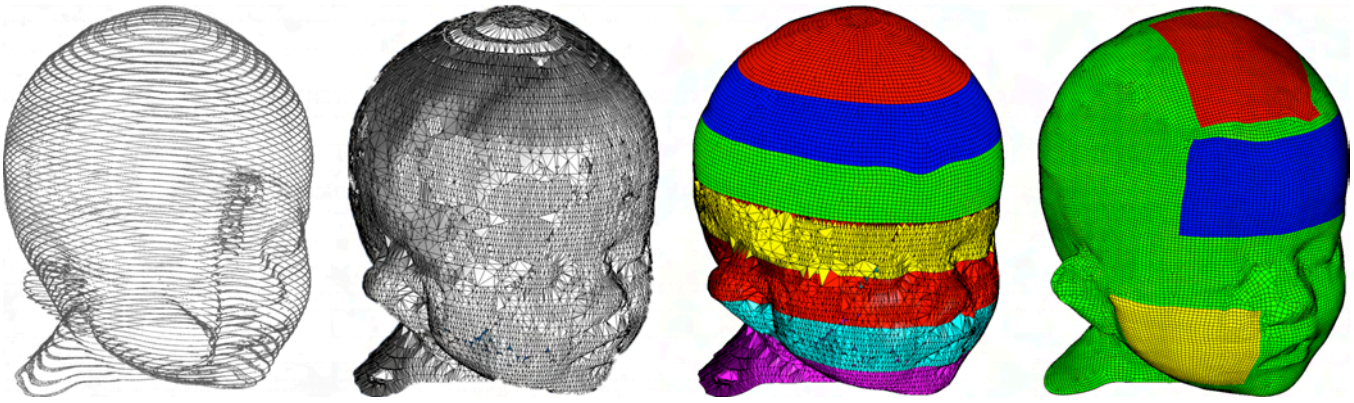

Fig. 6 Mesh generation from clinical images. From the computer tomography scans, we extract discrete point cloud data (left), which we filter and mesh using a ball-pivoting algorithm. This generates a triangular surface mesh, which is further smoothened (middle) and turned into a final volume mesh (right). The final discretization of the skull consists of 61,228 nodes, 183,684 degrees of freedom, and 30,889 tri-linear brick elements. We virtually implant three tissue expanders, one in the scalp, discretized with 4,356 nodes, 13,068 degrees of freedom, and 2,088 brick elements (red), one in the cheek, discretized with 2,542 nodes, 7,626 degrees of freedom, and 1,200 brick elements (yellow), and one in the forehead, discretized with 3,782 nodes, 11,346 degrees of freedom, and 1,800 brick elements (blue).

pansion case illustrated in Figure 1. First, we implant an expander in the scalp, discretized with 4,356 nodes, 13,068 degrees of freedom, and 2,088 tri-linear brick elements, covering an initial area of 50.4 cm^2, shown in red. Second, we implant an expander in the cheek, discretized with 2,542 nodes, 7,626 degrees of freedom, and 1,200 tri-linear brick elements, covering an initial area of 29.3 cm^2, shown in yellow. Third, we implant and expander in the forehead, discretized with 3,782 nodes, 11,346 degrees of freedom, and 1,800 tri-linear brick elements, covering an initial area of 48.5 cm^2, shown in blue. To simulate tissue expansion, we fix all nodes and release only the expander degrees of freedom, which we then pressurize from underneath.

3 Results

We illustrate the impact of tissue expansion at three characteristic locations of the skull, in the scalp, the forehead, and the cheek. For the elastic model, we assume Lamé constants of $\lambda = 0.7141$ MPa and $\mu = 0.1785$ MPa, which would correspond to a Poisson's ratio of $\nu = 0.4$ and a Young's modulus of E = 0.5 MPa in the linear regime [1, 52]. For the growth model, we assume a critical threshold of $\vartheta^{\text{crit}} = 1.1$, a maximum area growth of $\vartheta^{\max} = 4.0$, a growth exponent of $\gamma = 3.0$, and an adaptation speed of $1/\tau = 12$. We gradually pressurize the tissue expanders, $0.0 < t \leq 0.125$, then hold the pressure constant to allow the tissue to grow, $0.125 < t \leq 0.75$, and finally remove the pressure to visualize the grown area, $0.75 < t \leq 1.0$.

3.1 Tissue expansion in the scalp

Figures 7, 8, and 9 illustrate the tissue expansion process in the scalp. Figure 7 displays the temporal evolution of the normalized total area, elastic area, and growth area upon subsequent expander inflation, constant pressure, and expander removal. Once the elastic

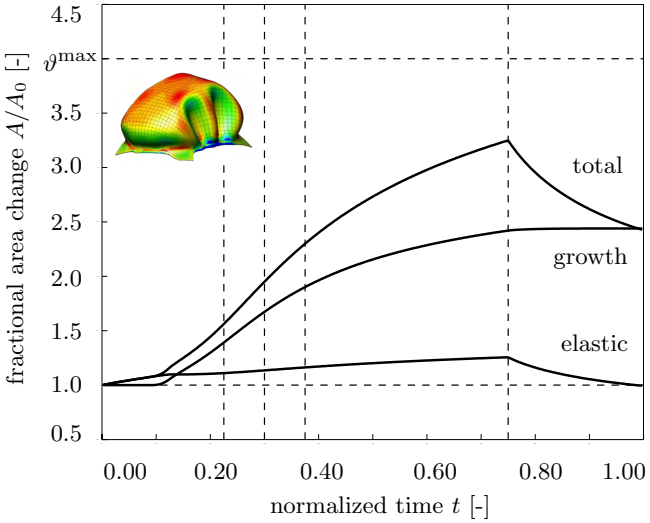

Fig. 7 Tissue expansion in the scalp. Temporal evolution of normalized total area, elastic area, and growth area upon gradual expander inflation, $0.0 < t \leq 0.125$, constant pressure $0.125 < t \leq 0.75$, and deflation $0.75 < t \leq 1.0$. The final fractional area gain is 2.44, corresponding to 122.8 cm^2. Vertical dashed lines correspond to the time points displayed in Figure 8.

area stretch reaches the critical threshold of $\vartheta^{\text{crit}} = 1.1$,

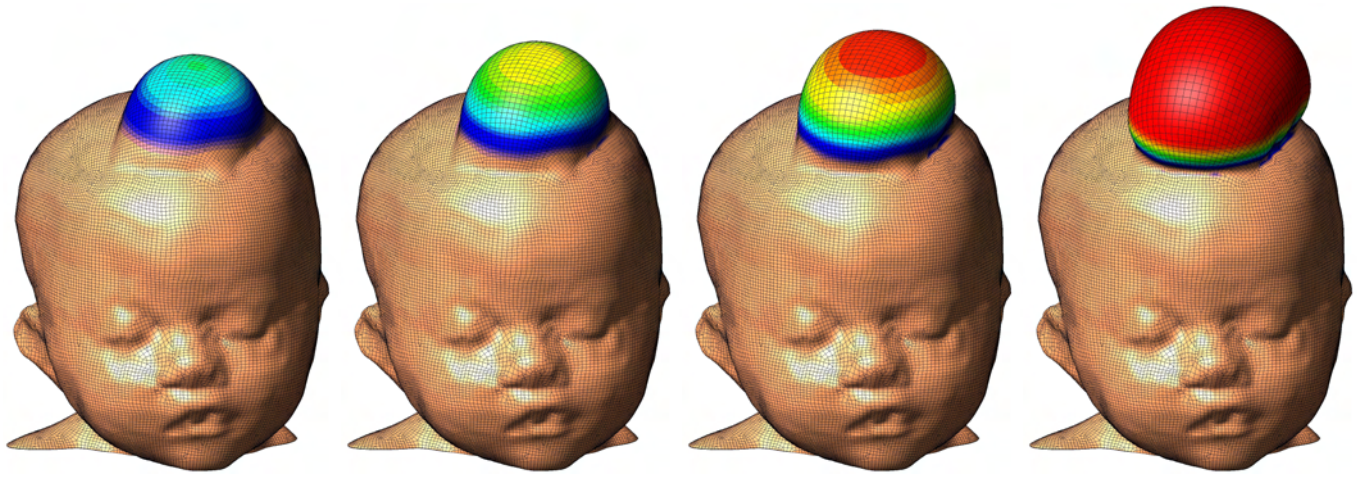

Fig. 8 Tissue expansion in the scalp. Spatio-temporal evolution of area growth displayed at $t = 0.225$, $t = 0.300$, $t = 0.375$ and $t = 0.750$. The initial area of $50.4\,\mathrm{cm}^2$ increases gradually as the grown skin area increases from $70.07\,\mathrm{cm}^2$, to $84.25\,\mathrm{cm}^2$, to $95.73\,\mathrm{cm}^2$, and finally to $121.87\,\mathrm{cm}^2$, from left to right.

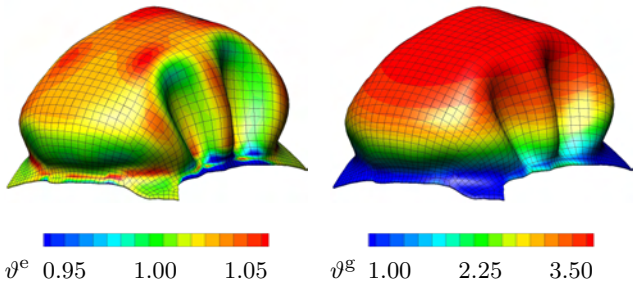

Fig. 9 Tissue expansion in the scalp. Remaining deformation upon expander removal. The elastic area strain of $0.95 \leq \vartheta^e \leq 1.05$ indicates an area change of $\pm 5\%$ giving rise to residual stresses (left). The area growth of $1.0 \leq \vartheta^g \leq 3.5$ shows that skin has more than doubled its initial area (right). The final fractional area gain is 2.44, corresponding to $122.8\,\mathrm{cm}^2$.

slightly before the total pressure is applied, at $t = 0.125$, the tissue starts to grow. As the expander pressure is held constant, growth increases gradually causing the total area to increase as well. Then, at $t = 0.75$, the pressure is decreased to remove the expander. The elastic area retracts gradually, while the grown area remains constant. The vertical dashed lines correspond to the discrete time points, $t = 0.225$, $t = 0.300$, $t = 0.375$ and $t = 0.750$, displayed in Figure 8. Figure 8 illustrates the spatio-temporal evolution of area growth ϑ^g. Growth is first initiated at the center of the expander, where the elastic stretch is largest. As growth spreads throughout the entire expanded area, the initial area of $50.4\,\mathrm{cm}^2$ increases gradually as the grown skin area increases from $70.07\,\mathrm{cm}^2$, to $84.25\,\mathrm{cm}^2$, to $95.73\,\mathrm{cm}^2$, and finally to $121.87\,\mathrm{cm}^2$, from left to right. Figure 9 summarizes the final outcome of the expansion in the scalp in terms of the remaining deformation upon expander removal. The elastic area strain of $0.95 \leq \vartheta^e \leq 1.05$ indicates an area change of $\pm 5\%$ giving rise to residual stresses, left. The area growth of $1.0 \leq \vartheta^g \leq 3.5$ shows that skin has more than doubled its initial area, right. This is in agreement with the final fractional area gain of 2.44, corresponding to an area growth in the scalp of $122.8\,\mathrm{cm}^2$.

3.2 Tissue expansion in the forehead

Figures 10, 11, and 12 summarize the tissue expansion process in the forehead. Figure 10 displays the temporal evolution of the normalized total area, elastic area, and growth area upon gradual expander inflation, constant pressure, and gradual expander removal. Similar to the expansion in the scalp, growth begins at stretches beyond the critical threshold level, then increases gradually upon constant pressure, and remains constant upon expander removal. Figure 11 illustrates the spatio-temporal evolution of area growth ϑ^g at four characteristic time points indicated through the vertical dashed lines in figure 10. The growth process starts in the center of the forehead and spreads out throughout the entire forehead area. As it does, the initial area of $48.5\,\mathrm{cm}^2$ increases gradually as the grown skin area increases from $66.56\,\mathrm{cm}^2$, to $76.54\,\mathrm{cm}^2$, to $85.96\,\mathrm{cm}^2$, and finally to $116.55\,\mathrm{cm}^2$, from left to right. Figure 12 displays the remaining deformation upon expander removal. The final fractional area gain during forehead expansion is 2.44, corresponding to an area growth of $118.1\,\mathrm{cm}^2$.

3.3 Tissue expansion in the cheek

Figures 13, 14, and 15 document the tissue expansion process in the cheek. Figure 13 summarizes the temporal evolution of the normalized total area, elastic area,

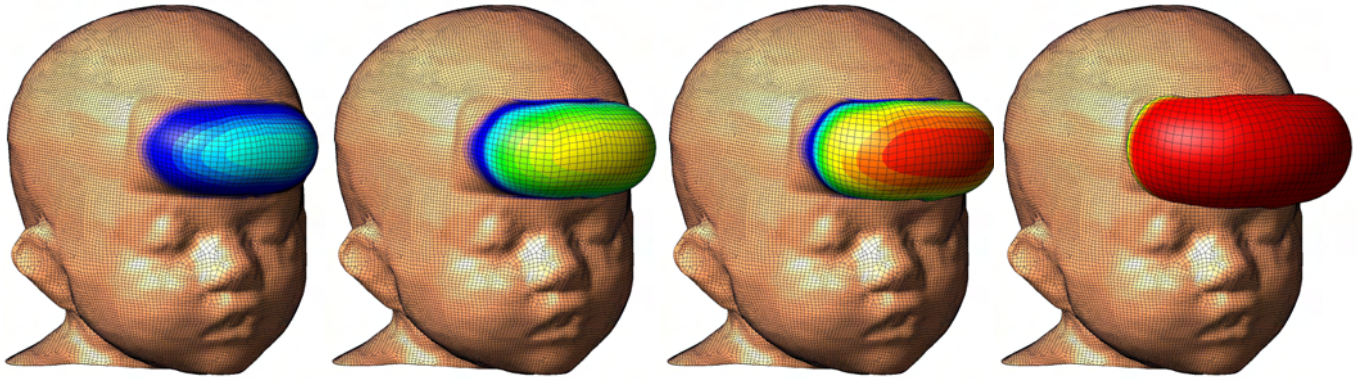

Fig. 11 Tissue expansion in the forehead. Spatio-temporal evolution of area growth displayed at $t = 0.225$, $t = 0.300$, $t = 0.375$ and $t = 0.750$. The initial area of $48.5\,\mathrm{cm}^2$ increases gradually as the grown skin area increases from $66.56\,\mathrm{cm}^2$, to $76.54\,\mathrm{cm}^2$, to $85.96\,\mathrm{cm}^2$, and finally to $116.55\,\mathrm{cm}^2$, from left to right.

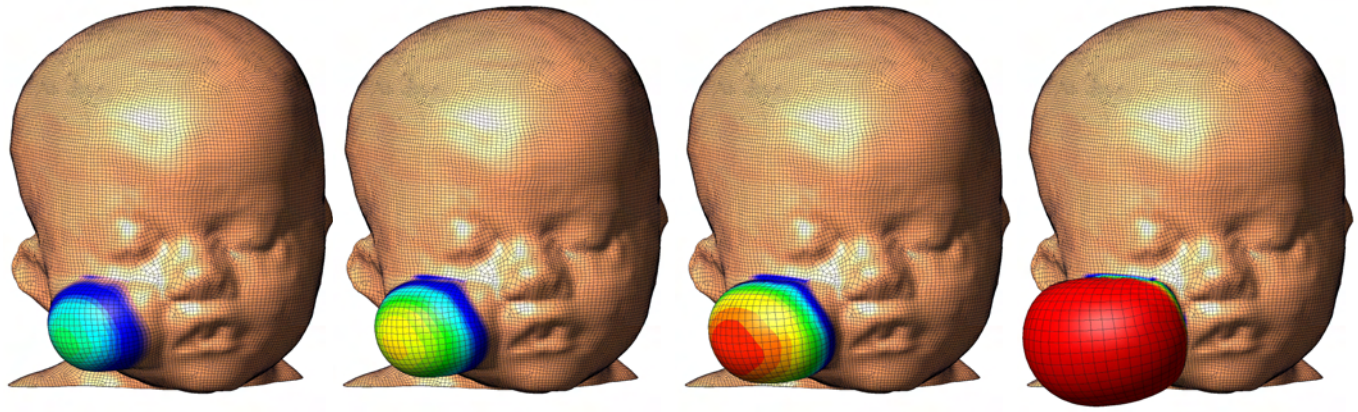

Fig. 14 Tissue expansion in the cheek. Spatio-temporal evolution of area growth displayed at $t = 0.225$, $t = 0.300$, $t = 0.375$ and $t = 0.750$. The initial area of $29.3\,\mathrm{cm}^2$ increases gradually as the grown skin area increases from $42.74\,\mathrm{cm}^2$, to $52.03\,\mathrm{cm}^2$, to $59.39\,\mathrm{cm}^2$, and finally to $76.86\,\mathrm{cm}^2$, from left to right.

and growth area upon gradual expander inflation, constant pressure, and gradual expander removal. Again, the growth process is initiated once the stretches reach the critical threshold of $\vartheta^{\mathrm{crit}} = 1.1$. Upon constant pressure, growth increases gradually. Upon pressure removal, growth remains constant displaying the irreversible nature of the growth process. Figure 14 illustrates the spatio-temporal evolution of area growth ϑ^{g} in the cheek. Again, growth begins in center of cheek, where the elastic area stretch is largest. As the growth process spreads out throughout the entire cheek area, the initial area of $29.3\,\mathrm{cm}^2$ increases gradually as the grown skin area increases from $42.74\,\mathrm{cm}^2$, to $52.03\,\mathrm{cm}^2$, to $59.39\,\mathrm{cm}^2$, and finally to $76.86\,\mathrm{cm}^2$, from left to right. Figure 15 summarizes the outcome of the expansion in the cheek with a final fractional area gain of 2.64, corresponding to an area growth of $77.4\,\mathrm{cm}^2$.

4 Discussion

Tissue expansion is one of the basic treatment modalities in modern reconstructive surgery. Inducing controlled tissue growth through well-defined overstretch, it creates skin that matches the color, texture, hair bearance, and thickness of the surrounding healthy skin, while minimizing scars and risk of rejection [21]. Despite its widespread use, the choice of the appropriate tissue expander is almost exclusively based on the surgeon's personal preference, and the discrepancy between recommended shapes, sizes, and volumes remains enormous [36]. The current gold standard for expander selection is to predict tissue growth by calculating the difference between the inflated and non-inflated expander surface [13, 53]. From an engineering point of view, it is quite intuitive, that this purely kinematic approach severely overestimates the net gain in surface area [60]. With a discrepancy of up to a factor four, these models assume that the entire deformation can be attributed to irreversible growth, completely neglecting the elastic deformation, which is reversible upon expander removal [36]. In an attempt

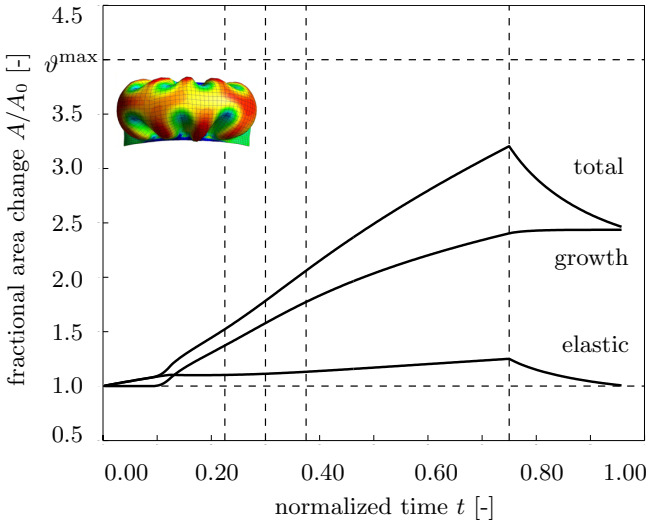

Fig. 10 Tissue expansion in the forehead. Temporal evolution of normalized total area, elastic area, and growth area upon gradual expander inflation, $0.0 < t \leq 0.125$, constant pressure $0.125 < t \leq 0.75$, and deflation $0.75 < t \leq 1.0$. The final fractional area gain is 2.44, corresponding to 118.1 cm^2. Vertical dashed lines correspond to the time points displayed in Figure 11.

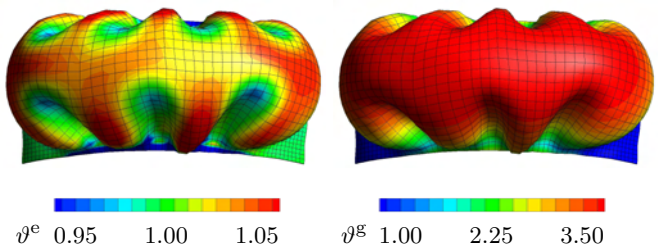

Fig. 12 Tissue expansion in the forehead. Remaining deformation upon expander removal. The elastic area strain of $0.95 \leq \vartheta^{\mathrm{e}} \leq 1.05$ indicates an area change of $\pm 5\%$ giving rise to residual stresses (left). The area growth of $1.0 \leq \vartheta^{\mathrm{g}} \leq 3.5$ shows that skin has more than doubled its initial area (right). The final fractional area gain is 2.44, corresponding to 118.1 cm^2.

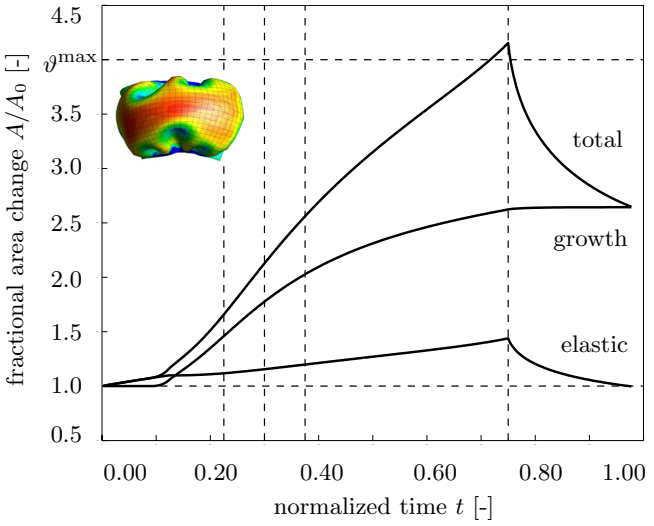

Fig. 13 Tissue expansion in the cheek. Temporal evolution of normalized total area, elastic area, and growth area upon gradual expander inflation, $0.0 < t \leq 0.125$, constant pressure $0.125 < t \leq 0.75$, and deflation $0.75 < t \leq 1.0$. The final fractional area gain is 2.64, corresponding to 77.4 cm^2. Vertical dashed lines correspond to the time points displayed in Figure 14.

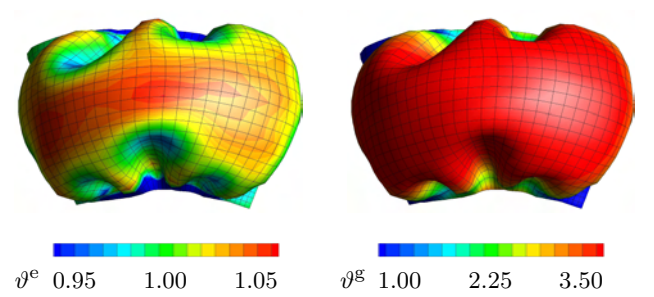

Fig. 15 Tissue expansion in the cheek. Remaining deformation upon expander removal. The elastic area strain of $0.95 \leq \vartheta^{\mathrm{e}} \leq 1.05$ indicates an area change of $\pm 5\%$ giving rise to residual stresses (left). The area growth of $1.0 \leq \vartheta^{\mathrm{g}} \leq 3.5$ shows that skin has more than doubled its initial area (right). The final fractional area gain is 2.64, corresponding to 77.4 cm^2.

to account for this error, empirical correction factors of 6.00, 3.75, and 4.50 have been proposed for circular, rectangular, and crescent-shaped expanders [60]. This demonstrates the vital need to rationalize criteria for a standardized device selection.

Motivated by a first study on axisymmetric skin growth [55], we have recently established a prototype model for growing membranes to simulate tissue expansion in a general three-dimensional setting [8]. We have applied our model to quantitatively compare four commonly available tissue expander geometries, round, square, rectangular, and crescent [9], however, only on initially flat geometries. Here, for the first time, we demostrate the potential of the model during tissue expansion in pediatric forehead reconstruction using a real patient-specific model. To embed the solution into a nonlinear finite element environment, we discretize the governing equations for in-plane area growth in time and space. To solve the nonlinear set of equations, we apply an incremental iterative Newton-Raphson solution strategy based on the consistent algorithmic linearization. The resulting algorithm is remarkably efficient, stable, and robust. It is capable of predicting tissue expander inflation, tissue growth, and expander deflation at different locations of a human skull within the order of minutes on a standard laptop computer. Because of its geometric flexibility, our general algorithm could also be adapted to predict tissue expansion in the trunk [4] or in the upper and lower extremities [20].

Although the proposed model for skin growth represents a significant advancement over the axisymmetric growth

model previously proposed [55], we would like to point out that some limitations remain. First, motivated by experimental observations, which report normal cell differentiation upon tissue expansion [61], we have assumed that the material microstructure remains unaffected by the growth process, $\boldsymbol{F}^{\mathrm{g}} = \sqrt{\vartheta^{\mathrm{g}}}\boldsymbol{I} + [1 - \sqrt{\vartheta^{\mathrm{g}}}]\boldsymbol{n}_0 \otimes \boldsymbol{n}_0$. Here, for the sake of simplicity, we have modeled this microstructure as isotropic and elastic. We have recently shown that it is straightforward combine our growth model with in-plane anisotropy, introduced through pronounced stiffness along Langer's lines [9, 30]. It might also be interesting to elaborate out-of-plane anisotropy and model the different skin layers individually [39]. We have demonstrated how to model the growth process itself as anisotropic as well [16]. This could imply growth $\vartheta^{||}$ exclusively along specific microstructural directions such as Langer's lines, $\boldsymbol{F}^{\mathrm{g}} = \boldsymbol{I} + [\vartheta^{||} - 1]\boldsymbol{\nu}_0^{||} \otimes \boldsymbol{\nu}_0^{||}$, or major in-plane growth $\vartheta^{||}$ along Langer's lines combined with minor in-plane growth $\vartheta^{\perp}$ orthogonal to Langer's lines, $\boldsymbol{F}^{\mathrm{g}} = \vartheta^{||}\,\boldsymbol{\nu}_0^{||} \otimes \boldsymbol{\nu}_0^{||} + \vartheta^{\perp}\,\boldsymbol{\nu}_0^{\perp} \otimes \boldsymbol{\nu}_0^{\perp} + \boldsymbol{n}_0 \otimes \boldsymbol{n}_0$. Similarly, we could even introduce a progressive reorientation of the collagen network to allow for the material to align with the maximum principal strains [33, 42]. Ideally, the growth law would be tied to the underlying mechanobiology [11]. Comparative tissue histology of grown and ungrown tissue samples could help to identify the mechanisms that trigger skin growth to validate or, if necessary, refine our evolution equation (13) for the growth tensor.

Second, for the sake of simplicity, our finite element mesh consists of one single brick element with two integration points across the skin thickness. We have previously studied the sensitivity of growth with respect to thickness refinement using a higher resolution across the thickness [8, 9]. However, our results were rather insensitive to mesh refinement. This insensitivity might be explained by the fact that, upon expander inflation, the skin is almost in a pure membrane state. During deflation, however, we observe buckling associated with strain gradients across the skin thickness, which might play a critical role in the development of residual stresses. To explore these residual stresses further, we are currently refining our model utilizing a shell kinematics [47] with a higher resolution across the thickness direction. This will also allow us to simulate the individual skin layers [35, 54] and their interaction during the expansion process, which we believe to be a major source of residual stress in real tissue expansion cases [41, 62].

Third, for the sake of simplicity, we have modeled tissue expansion only implicitly through controlling the applied pressure. In real tissue expansion, the external control parameter is the expander volume [36]. This implies that our virtual tissue expansion displays creep under constant loading, while clinical tissue expansion might rather display relaxation under constant deformation [9], similar to our parameter study in Figure 4.

Fourth, here, we have assumed that the expander is connected tightly to the expanded tissue, neglecting effects of interface sliding and shear [55]. This seems to be a reasonable first assumption though, since most current expanders have well-designed textures to promote mild tissue in-growth, primarily to prevent expander migration [6]. To address these potential limitations, we are currently refining the elastic model, the growth model, and the boundary conditions, to render our future simulations more realistic.

Last, while our computational model seems well suited to provide qualitative guidelines and trends, at its present state, it is not recommended for quantitative statements. We will need to perform acute and chronic in vitro and in vivo experiments to truly calibrate the underlying material parameters, to potentially refine and fully validate our model, to eventually make it applicable for clinical practice. Nevertheless, we believe that using the equations on nonlinear continuum mechanics represents a significant advancement over the current gold standard to predict tissue growth exclusively in terms of kinematic quantities [53, 60].

Conclusion

We have presented a novel computational model to predict the chronic adaptation of thin biological membranes when stretched beyond their physiological limit. Here, to illustrate the features of this model, we have demonstrated its performance during tissue expansion in pediatric forehead reconstruction. We have quantified reversibly elastic and irreversibly grown area changes in response to skin expansion in the scalp, the forehead, and the cheek of a one-year-old child. In general, our generic computational model is applicable to arbitrary skin geometries, and has the potential to predict area gain in skin expansion during various common procedures in reconstructive surgery. A comprehensive understanding of the gradually evolving stress and strain fields in growing skin may help the surgeon to prevent tissue damage and optimize clinical process parameters such as expander geometry, expander size, expander placement, and inflation timing. Ultimately, through inverse modeling, computational tools like ours have the potential to rationalize these parameters to create skin flaps of desired size and shape. Overall, we believe that predictive computational modeling might open new avenues in reconstructive surgery and enhance treatment for patients with birth defects, burn injuries, or breast tumor removal.

Acknowledgements

This work was supported by the Claudio X. Gonzalez Fellowship CVU 358668 and the Stanford Graduate Fellowship to Adrián Buganza Tepole and by the

National Science Foundation CAREER award CMMI-0952021 and the National Institutes of Health Grant U54 GM072970 to Ellen Kuhl.

References

1. Agache PG, Monneur C, Leveque JL, DeRigal J. Mechanical properties and Young's modulus of human skin in vivo. *Arch Dermatol Res.* 1980;269:221-232.
2. Ambrosi D, Ateshian GA, Arruda EM, Cowin SC, Dumais J, Goriely A, Holzapfel GA, Humphrey JD, Kemkemer R, Kuhl E, Olberding JE, Taber LA, Garikipati K. Perspectives on biological growth and remodeling. *J Mech Phys Solids.* 2011;59:863-883.
3. Argenta LC, Watanabe MJ, Grabb WC. The use of tissue expansion in head and neck reconstruction. *Annals Plast Surg.* 1983;11:31-37.
4. Arneja JS, Gosain AK. Giant congenital melanocytic nevi of the trunk and an algorithm for treatment. *J Craniofac Surg.* 2005;16:886-893.
5. Arneja JS, Gosain AK. Giant congenital melanocytic nevi. *Plast Reconstr Surg.* 2007;120:26e-40e.
6. Barone FE, Perry L, Keller T, Maxwell GP. The biomechanical and histopathologic effect of surface texturing with silicone and polyurethane in tissue implantation and expansion. *Plast Reconstr Surg.* 1992;90:77-86.
7. Bernardini F, Mittleman J, Rushmeiner H, Silva C, Taubin G. The ball-pivoting algorithm for surface reconstruction. *IEEE Trans Vis Comp Graph.* 1999;5:349-359.
8. Buganza Tepole A, Ploch CJ, Wong J, Gosain AK, Kuhl E. Growing skin - A computational model for skin expansion in reconstructive surgery. *J Mech Phys Solids.* 2011;59:2177-2190.
9. Buganza Tepole A, Gosain AK, Kuhl E. Stretching skin: The physiological limit and beyond. *Int J Nonlin Mech.* doi: 10.1016/j.ijnonlinmec.2011.07.006.
10. Castilla EE, da Graca Dutra M, Orioli-Parreiras IM. Epidermiology of congenital pigmented naevi: I. Incidence rates and relative frequencies. *Br J Dermatol.* 1981;104:307-315.
11. De Filippo RE, Atala A. Stretch and growth: the molecular and physiologic influences of tissue expansion. *Plast Reconstr Surg.* 2002;109:2450-2462.
12. Dervaux J, Ciarletta P, Ben Amar M. Morphogenesis of thin hyperelastic plates: A constitutive theory of biological growth in the Föppl-von Karman limit. *J Mech Phys Solids.* 2009;57:458-471.
13. Duits EHA, Molenaar J, van Rappard JHA. The modeling of skin expanders. *Plast Reconstr Surg.* 1989;83:362-367.
14. Epstein M, Maugin GA. Thermomechanics of volumetric growth in uniform bodies. *Int J Plast.* 2000;16:951-978.
15. Garikipati K. The kinematics of biological growth. *Appl Mech Rev.* 2009;62:030801.1-030801.7.
16. Göktepe S, Abilez OJ, Parker KK, Kuhl E. A multiscale model for eccentric and concentric cardiac growth through sarcomerogenesis. *J Theor Bio.* 2010;265:433-442.
17. Göktepe S, Abilez OJ, Kuhl E. A generic approach towards finite growth with examples of athlete's heart, cardiac dilation, and cardiac wall thickening. *J Mech Phys Solids.* 2010;58:1661-1680.
18. Goriely A, BenAmar M. Differential growth and instability in elastic shells. *Phys Rev Letters.* 2005;94:198103.
19. Goriely A, BenAmar M. On the definition and modeling of incremental, cumulative, and continuous growth laws in morphoelasticity. *Biomech Model Mechanobio.* 2007;6:289296.
20. Gosain AK, Santoro TD, Larson DL, Gingrass RP. Giant congenital nevi: A 20-year experience and an algorithm for their management. *Plast Reconstr Surg.* 2001;108:622-636.
21. Gosain AK, Zochowski CG, Cortes W. Refinements of tissue expansion for pediatric forehead reconstruction: A 13-year experience. *Plast Reconstr Surg.* 2009;124:1559-1570.
22. Himpel G, Kuhl E, Menzel A, Steinmann P. Computational modeling of isotropic multiplicative growth. *Comp Mod Eng Sci.* 2005;8:119-134.
23. Kaplan EN. The risk of malignancy in large congenital nevi. *Plast Reconstr Surg.* 1974;53:421-428.
24. Kobbelt LP, Vorsatz J, Labsik U, Seidel HP. A shrink wrapping approach to remeshing polygonal surfaces. *Comp Graph Forum.* 1999;18:119-130.
25. Kroon W, Delhaas T, Arts T, Bovendeerd P. Computational modeling of volumetric soft tissue growth: Application to the cardiac left ventricle. *Biomech Model Mechanobio.* 2009;8:310-309.
26. Kuhl E, Steinmann P. Mass- and volume specific views on thermodynamics for open systems. *Proc Royal Soc.* 2003;459:2547-2568.
27. Kuhl E, Steinmann P. On spatial and material settings of thermohyperelstodynamics for open systems. *Acta Mech.* 2003;160:179-217.
28. Kuhl E, Menzel A, Steinmann P. Computational modeling of growth - A critical review, a classification of concepts and two new consistent approaches. *Comp Mech.* 2003;32:71-88.
29. Kuhl E, Steinmann P. Computational modeling of healing - An application of the material force method. *Biomech Model Mechanobio.* 2004;2:187-203.
30. Kuhl E, Garikipati K, Arruda EM, Grosh K. Remodeling of biological tissue: Mechanically induced reorientation of a transversely isotropic chain network. *J Mech Phys Solids.* 2005;53:1552-1573.
31. Kuhl E, Menzel A, Garikipati K. On the convexity of transversely isotropic chain network models. *Phil Mag.* 2006;86:3241-3258.
32. Kuhl E, Maas R, Himpel G, Menzel A. Computational modeling of arterial wall growth: Attempts towards patient-specific simulations based on computer tomography. *Biomech Model Mechanobio.* 2007;6:321-331.
33. Kuhl E, Holzapfel GA. A continuum model for remodeling in living structures. *J Mat Sci.* 2007;2:8811-8823.
34. Lee EH. Elastic-plastic deformation at finite strains. *J Appl Mech.* 1969;36:1-6.
35. Levi K, Kwan A, Rhines AS, Gorcea M, Moore DJ, Dauskardt RH. Emollient molecule effects on the drying stresses in human stratum corneum. *Brit J Dermatol.* 2010;163:695-703.
36. LoGiudice J, Gosain AK. Pediatric tissue expansion: Indications and complications. *J Craniofac Surg.* 2003;14:866-872.

37. Lubarda VA, Hoger A. On the mechanics of solids with a growing mass. *Int J Solids & Structures.* 2002;39:4627-4664.
38. Lubarda VA. Constitutive theories based on the multiplicative decomposition of deformation gradient: Thermoelasticity, elastoplasticity and biomechanics. *Appl Mech Rev.* 2004:57;95108.
39. Mazza E, Papes O, Rubin MB, Bodner SR, Binur NS. Nonlinear elastic-viscoplastic constitutive equations for aging facial tissues. *Biomech Model Mechanobiol.* 2005;4:178-189.
40. McMahon J, Goriely A. Spontaneous cavitation in growing elastic membranes. *Math Mech Solids.* 2010;15:57-77.
41. Menzel A. Modelling of anisotropic growth in biological tissues - A new approach and computational aspects. *Biomech Model Mechanobiol.* 2005;3:147-171.
42. Menzel A. A fibre reorientation model for orthotropic multiplicative growth. *Biomech Model Mechanobiol.* 2007;6:303-320.
43. Neumann CG. The expansion of an area of skin by progressive distension of a subcutaneous balloon; use of the method for securing skin for subtotal reconstruction of the ear. *Plast Reconstr Surg.* 1959;19:124-130.
44. Pang H, Shiwalkar AP, Madormo CM, Taylor RE, Andriacchi TP, Kuhl E. Computational modeling of bone density profiles in response to gait: A subject-specific approach. *Biomech Model Mechanobio.* doi: 10.1007/s10237-011-0318-y.
45. Quaba AA, Wallace AF. The incidence of malignant melanoma (0 to 15 years of age) arising in large congenital nevocellular nevi. *Plast Reconstr Surg.* 1986;78:174-178.
46. Radovan C. Breast reconstruction after mastectomy using the temporary expander. *Plast Reconstr Surg.* 1982;69:195-208.
47. Rausch MK, Bothe W, Kvitting JP, Göktepe S, Miller DC, Kuhl E. In vivo dynamic strains of the ovine anterior mitral valve leaflet. *J Biomech.* 2011;44:1149-1157.
48. Rausch MK, Dam A, Göktepe S, Abilez OJ, Kuhl E. Computational modeling of growth: Systemic and pulmonary hypertension in the heart. *Biomech Model Mechanobiol.* doi:10.1007/s10237-010-0275-x.
49. Rivera R, LoGiudice J, Gosain AK. Tissue expansion in pediatric patients. *Clin Plast Surg.* 2005;32:35-44.
50. Rodriguez EK, Hoger A, McCulloch AD. Stress-dependent finite growth in soft elastic tissues. *J Biomech.* 1994;27:455-467.
51. Schmid H, Pauli L, Paulus A, Kuhl E, Itskov M. How to utilise the kinematic constraint of incompressibility for modelling adaptation of soft tissues. *Comp Meth Biomech Biomed Eng.* doi: 10.1080/10255842.2010.548325.
52. Serup J, Jemec GBE, Grove GL. Handbook of Non-Invasive Methods and the Skin. Informa Healthcare. 2003.
53. Shively RE. Skin expander volume estimator. *Plast Reconstr Surg.* 1986;77:482-483.
54. Silver FH, Siperko LM, Seehra GP. Mechanobiology of force transduction in dermal tissue. *Skin Res Tech.* 2003;9:3-23.
55. Socci L, Pennati G, Gervaso F, Vena P. An axisymmetric computational model of skin expansion and growth. *Biomech Model Mechanobiol.* 2007;6:177-188.
56. Taber LA. Biomechanics of growth, remodeling and morphogenesis. *Appl Mech Rev.* 1995;48:487-545.
57. Takei T, Mills I, Arai K, Sumpio BE. Molecular basis for tissue expansion: Clinical implications for the surgeon. *Plast Reconstr Surg.* 1998;102:247-258.
58. Taylor RL. FEAP - A Finite Element Analysis Program. *Version 8.3, User Manual*, University of California at Berkeley, 2011.
59. van der Kolk CA, McCann JJ, Knight KR, O'Brien BM. Some further characteristics of expanded tissue. *Clin Plast Surg.* 1987;14:447-453.
60. van Rappard JHA, Molenaar J, van Doorn K, Sonneveld GJ, Borghouts JMHM. Surface-area increase in tissue expansion. *Plast Reconstr Surg.* 1988;82:833-839.
61. Wollina U, Berger U, Stolle C, Stolle H, Schubert H, Zieger M, Hipler C, Schumann D. Tissue expansion in pig skin - A histochemical approach. *Anat Histol Embryol.* 1992;21:101-11.
62. Wu KS, van Osdol WW, Dauskardt RH. Mechanical properties of human stratum corneum: Effects of temperature, hydration, and chemical treatment. *Biomaterials.* 2006;27:785-795.
63. Zeng Y, Xu C, Yang J, Sun G, Xu X. Biomechanical comparison between conventional and rapid expansion of skin. *Brit Assoc Plast Surg.* 2003;56:660-666.